CrystEngComm

Accepted Manuscript

ROYAL SOCIETY OF CHEMISTRY

www.rsc.org/crystengcomm

Nanocrystallization in magnetron sputtered Zr-Cu-Al-Ag thin film metallic glasses

S.Thanka Rajan, A.K.Nandakumar, B.Subramanian*

Electrochemical Materials Science Division,

CSIR-Central Electrochemical Research Institute, Karaikudi-630 006, India.

Abstract

Zr-based thin film metallic glasses (TFMG) were fabricated from a polycrystalline $Zr_{48}Cu_{36}Al_8Ag_8$ (at.%) target by DC magnetron sputtering. A series of characterization techniques were employed to study the structure, composition and thermal stability of the glassy coating and also the mechanical compliance of the TFMG over stainless steel. X-ray diffraction indicated a completely amorphous microstructure. However, specimens prepared for plan-view TEM revealed nanocrystallites of the $CuZr_2$ phase dispersed in an amorphous matrix. Annealing experiments showed that the primary phase to nucleate in the films is the $CuZr_2$ phase as observed from XRD. The film/substrate interface did not show any inter-diffusion, as confirmed by high resolution scanning TEM. Calorimetric studies by DSC showed a large supercooled liquid region of about 83 K. Surface morphological studies by both FE-SEM and AFM indicated a very smooth surface devoid of pores or cracks, with an average roughness of about 1.25 nm. X-ray photo-electron spectroscopy (XPS) showed oxygen on the film surface; both Zr and Al also revealed non-metallic bonding peaks concomitant with a mixed or bilayer oxide on the surface. A very high scratch resistance was observed for the specimen coated over stainless steel substrates.

Key words: Thin film metallic glasses, sputtering, amorphous material, structural Properties

Corresponding author email: bsmanian@cecri.res.in (B.Subramanian)

1. Introduction

The discovery of metallic glasses (MG) has stimulated widespread research because of their technological and scientific importance in understanding the science of glass formation. Metallic glasses are characterized by short range order compared to Crystalline solids that have long range order of the atom [1]. The absence of a poly crystalline microstructure in metallic glasses obviates or at the least delays material failure occurring at or through normal lattice defects and grain boundaries - like crack propagation and pitting corrosion [2]. Consequently, their isotropic mechanical properties, high corrosion resistance and absence of segregation make them highly feasible for various applications [3]. Yet, commercial production and real scale application of such bulk metallic glasses (BMG) have been impeded largely owing to the difficulty in producing BMGs of suitable sizes – often it is hard to produce a BMG sheet thicker than 10 mm. The critical cooling rate required to freeze a liquid melt without inducing any crystallization scales inversely as the square of the thickness ($1/t^2$) and proportionally with the thermal diffusivity of the specimen (κ): $\dot{T}_{cr} \propto \kappa/t^2$. For nominal values of κ, critical cooling rates vary between 150-1 K/s or lower [4]. Therefore, both thickness and thermal diffusivity of the specimen are crucial to obtain a homogenous BMG component.

Both metallic alloys and metal-metalloids (B, Si, P, N) mixtures have been investigated and reported to form glassy structures. Among the metallic BMG, Zr-based ternary Zr-Cu-Ni alloys are usually characterized by their superior glass forming ability (GFA), with $\dot{T}_{cr}$ as low as 1 K s^{-1}, a large super cooled liquid region exceeding 100 K and good engineering properties [5]. Zr based BMG have a reported tensile strength of about

1800MPa, Vickers hardness (HV) of 500-600, fracture toughness between 16-55 MPa. $m^{1/2}$ and density of 5900–6700kg/m^3at room temperature [6-8].

Recently, efforts have shifted to replace Ni by Al in the Zr-Cu BMG since Ni is a known carcinogenic toxin. Zhang et al reported for the first time that a particular combination of $Zr_{48}Cu_{36}Al_8Ag_8$ was found to lie exactly at the quaternary eutectic point and showed a maximal glass formability leading to rod diameters of nearly 25 mm. They fabricated a series of Zr-Cu-Al-Ag alloys whose large glass forming ability allowed the mould casting of BMG rods with diameters of 15 mm [9]. This new composition alloys were more environmentally benign and did not pose a health hazard as did Ni-based BMG. Similar studies on the Zr-Cu-Al-Ag BMG were conducted by Jiang and co-workers [10]. Through structural and thermal characterizations, they showed that compositions very near to $Zr_{46}Cu_{38}Al_8Ag_8$ show excellent glass formability and a large super cooled liquid region in addition to high strength and corrosion resistance in sulphuric acid. This eutectic composition of $Zr_{48}Cu_{36}Al_8Ag_8$ has proved versatile for alloying with Si and other transition metals like Ta leading to nano-crystallite dispersion strengthened BMG, which show good strength, improved ductility and excellent weldability with other BMG plates and also with pure Al sheets, without any detectable phase segregation at the weld joints [11-13].The presence of Al in Zr-Cu based metallic glasses also provides surface passivation under corrosive environments by formation of ZrO_2/Al_2O_3 oxide bilayers. Introduction of small amounts of Ag in the system seems to induce a two-step crystallization sequence, and also a decrease of the crystallization temperature [14]. Excessive amounts of Ag and Al tend to reduce T_g substantially. Fabricating Zr-Cu-Al-Ag BMG are challenging in another aspect, in that generally negative heats of mixing of components increases the thermal stability of metallic glasses, but in this case, Cu-Ag has positive heat of mixing ($\Delta H_{mix}>0$) and is therefore susceptible to phase separation. The miscibility gap occurs at $T\leq780$ K, and under large super-cooling, the phase

separation can occur spontaneously to Ag and Cu clusters, which have been observed in previous reports [15].

In recent times, methods of condensing atoms from the vapour phase have also been reported to form non-crystalline layers on crystalline substrates. Unlike a continuously cooled melt, these systems are forced into a steep energy gradient by phase transitioning directly from a vapour to solid circumventing the intermediate liquid phase. Such amorphous phases with compositions nearly similar to their BMG counterparts are now termed as thin film metallic glasses (TFMG), and often times they serve the purpose of BMG albeit with the support of the underlying substrate. Thin film deposition techniques such as sputtering, laser deposition and arc plasma deposition are capable of producing atomic species that are far from equilibrium and have been employed to produce metallic glass films [16-18], with reasonable homogeneity, compositional uniformity, negligible interfacial reactivity and good adhesion over various substrates [19,20]. Coatings of metallic glasses over stainless steel and other important materials also provide an easy route to circumvent the manufacturing hurdles associated with BMG, and yet obtain the desired properties of metallic glasses. Particularly, applications in which surface properties are essential, for instance in biomedical implants or corrosion inhibition, can be greatly improved by TFMG coatings over mechanically compliant substrates [21].

In the context of TFMG, it should be pointed out that while the Zr-Cu-Al-Ag BMG alloy and the particular eutectic composition of $Zr_{48}Cu_{36}Al_8Ag_8$ has spawned a number of research reports on the mechanical, thermal and structural aspects of the alloy, reports on the microstructure, thermal and mechanical attributes of thin films of the eutectic or near eutectic $Zr_{48}Cu_{36}Al_8Ag_8$ metallic glasses have been rather scarce in the literature. There are many challenges with obtaining TFMG – primarily the energy of the vapour condensed film is quite high and secondly, stray gas atoms like Oxygen and Nitrogen are incorporated into the film

structure during growth. Although surface passivation by oxidation and nitridation are beneficial for corrosion inhibition, it is often found oxygen is gettered into the film. Interestingly, such gettered oxygen in Zr-based BMG often leads to quasi/icosahedral crystal nucleation in the amorphous matrix [22]. Particularly in the Zr-Cu-Al system, the icosahedral phase is one of a two stage crystallization mode; the quasicrystals form prior to the precipitation of the first stable phase. While such studies exist for $Zr_{48}Cu_{36}Al_8Ag_8$ BMG, information pertaining to compositional homogeneity, structural evolution and crystallization and adhesion properties on thin film form of nearly equal composition will be useful for applications such as corrosion inhibiting coatings, bio implantable coatings and surface protection of steels and other metallic alloys.

This paper reports a detailed study on the thermal, structural and compositional characterization of Zr-Cu-Al-Ag TFMG prepared by DC magnetron sputtering over Si substrates. Both the surface and the film/substrate interface were analyzed using conventional and scanning TEM. Mechanical characterization on films coated over stainless steel substrates were also carried out.

2. Experimental

2.1. Preparation of Zr- based TFMG

A sputtering target of $Zr_{48}Cu_{36}Al_8Ag_8$ (at.%) alloy was prepared by the vacuum arc-melting technique. The appropriate amount of pure metals (99.99% purity) of Zr, Cu, Al, and Ag was weighed, and arc melted under an argon atmosphere in a water-cooled copper die. The arc-melting was performed many times to obtain a uniform distribution of all the elements in the target. The composition of the target using EDAX analysis was found to be $Zr_{48}Cu_{36}Al_8Ag_8$ (at.%) which was in excellent agreement with the initial precursors used. The target was polycrystalline, as confirmed by X-ray diffraction. This $Zr_{48}Cu_{36}Al_8Ag_8$specimen was cut and polished to the required dimensions (50 mm diameter, and 3 mm thick) to suit

the target holder; Zr-Cu-Al-Ag thin films were then deposited on single crystal Si (100) oriented wafer substrates, glass and also on 316L stainless steel substrates using a DC magnetron sputtering system. The sputtering conditions employed for the preparation of the TFMGs are given in Table 1. Prior to deposition, the sputtering chamber was evacuated to a base pressure of 3×10^{-6} mbar, and high purity argon gas (grade-1) was used as the sputtering gas. The deposited films were annealed at 550 ºC (823 K) for 10 minutes inside the vacuum chamber.

2.2 Characterization of the TFMGs

Thermal characterization of the coatings was carried out using a differential scanning calorimeter (DSC) from TA Instruments (Model SDT Q600). The structure of the coatings was examined by a Bruker D8 Advance X-ray diffractometer operating in the Bragg-Brentano mode. Further characterizations were carried out using a TEM. Two types of samples were prepared – one a plan-view sample and another cross-section sample to study the film/substrate interface. For the plan-view specimen, a spalled-off foil was carefully separated from the substrate and stuck to a crab-type copper grid. The fragile foil was then directly thinned from both top and bottom sides to electron transparency by Ar ion milling at a relatively low energy (4 kV). The milling was halted every 30 minutes and allowed to rest for 30 minutes before resuming, to avoid heat-up during ion bombardment. After a few such cycles, a hole was visible at which point the milling was stopped and the sample taken out immediately for the TEM analysis. Cross-section TEM specimens were prepared by focused ion beam (FIB) machining in a Hitachi FB-2000 instrument capable of both Ga ion machining and electron imaging. The thin film sample was mounted on a semiconductor support grid and a protective layer of tungsten was deposited over the region of interest. Two trenches were milled away in such a way that a thin wall is left between the two trenches; the

wall being thin enough to be electron-transparent when tilted by 90º. Care was taken to conduct the ion milling at low energies to avoid beam-induced damage. No curtaining artefacts were observed on the specimen after the machining process. The thinned specimens were examined in a JEOL-JSM 2100F field emission transmission electron microscope (TEM) operating in scanning (STEM) mode. Chemical analyses were carried out by using the X-ray energy dispersive spectral analysis (XEDS) attachment available with the instrument. A Si (Li) detector equipped with drift detection was used for EDS mapping. Collection range of the detector was 0-20 keV and the dead time monitored was comfortably below 8%. The surface morphology of the prepared films was studied using a Zeiss FESEM. EDAX analysis was carried out in a TESCAN SEM, fitted with a Bruker Quantax EDS detector and Esprit 1.9 software. Atomic force microscopy (AFM) for topographic studies was done by Agliant technologies (model 5500).

2.3. Mechanical characterization:

Thickness of the TFMG specimen was measured using Calo test. Stainless steel balls of specified diameter were rotated on samples and two concentric circles were formed. Coating thickness was determined with the help of Calotest software and microscope arrangement on Micro-Combi Tester. The test has been performed in a micro scratch test system (Micro-Combi Tester, M/s. CSM Instruments, USA). A linearly progressive normal load was applied with a Rockwell (Diamond) indenter of 100μm radius. The test conditions were fixed to those values which give reproducible scratch maps. The starting load was 0.03N (default value), with a loading rate 25N/min. The final load and scratch length were selected so that total de-lamination occurs during the scratch process. Testing was performed over a scratch length of 4 mm at a speed of10mm/min, with a final load value of 15N. The critical loads for first crack event (Lc1), first de-lamination (Lc2) and total de-lamination (Lc3) were determined by means of the frictional force and acoustic emission data.

3. Results and discussion

3.1. Thermal characterization

Figure 1a shows the DSC curves of the Zr-Cu-Al-Ag TFMG. They exhibit an endothermic heat event characteristic of glass transition followed by an exothermic heat release event. The heat release indicates the stepwise transformation from metastable super cooled liquid region to the crystallization region. The glass transition temperature (T_g) and first crystallization temperature (T_x) were at 330.22 °C (603.22 K) and 413.19 °C (686.13 K). The amorphous Zr- based TFMG exhibits a wide super cooled liquid region (ΔT_x) of 82.97 °C. The rather wide super cooled liquid region (ΔT_x) of about 83 °C (83 K) indicates the high thermal stability and high stabilization against crystallization. The crystallization enthalpy ΔH of the sample was calculated to be 1.437 kJ/g. The enthalpy of the super cooled liquid region was found to be 18.71 J/g. The exothermic peak (T_p) at 488.81 °C (761.81 K) is attributed to phase separation and primary crystallization. Often, rather than the T_g or the T_x value, the reduced glass transition temperature, $T_{rg}= (T_g/T_l)$ is used as an indicator of the alloy to form metallic glasses. $T_{rg}>2/3$ is usually employed as a thumb rule to predict glass formability of BMGs. However, in TFMG, this criterion is frequently relaxed owing to compositional deviation, condensation from the vapour phase and adatom mobility on the substrate surface. The Fig (1b) shows the DSC curve at higher temperatures, clearly indicating the endothermic melting peak at 931.19 °C (1204.19 K).The melting temperature (T_m) and liquidus temperature (T_l) are therefore 909.39 °C (1182.39 K) and 950.83 °C (1223.83 K). The T_{rg} and γ parameter ($\gamma= T_x/ (T_g+T_l)$) which are the thermal criteria for evaluating the glass forming ability of the alloy are determined as 0.3473 and 0.3225. The T_{rg} calculated for the TFMG is lower than its BMG counterpart (0.6) [26].

Figs. (2a, 2b) show the T_x and T_g values of various Zr-based BMG collected from a review of existing literature. The addition of Al and Ag to Zr-Cu BMG is observed to

increase the crystallization temperature and lower the glass transition temperature. The super cooled liquid region (ΔT_x) was also high indicating their high thermal stability. The corresponding values calculated for the present TFMG indicates a very low T_g in comparison with the BMG; however, they also show a low T_x when compared with Zr-Cu-Al-Ag BMG.

3.3 Compositional analysis

The SEM-EDAX spectrum (Fig. 3) shows the uniform distribution of elements in the TFMG and their concentration data clearly reveals the presence of Zr, Cu, Al and Ag. Quantification of the data yielded values for the amorphous film as Zr (48.28 at%), Cu (36.63 at%), Al (9.85 at%), Ag (5.24 at%). The EDAX measurement in different surface areas of the TFMG revealed almost the same concentration but not the exact concentration in all the different measured areas. There is a difference observed in the composition of the sputtering target and the sputtered thin film. The concentrations of Zr and Cu were slightly increased and Ag and Al are decreased. The sputtering yield of the various elements in the alloy target varies with atomic mass and binding energy of the elements. Moreover, the scattering in the plasma varies with the scattering cross section of the sputtered species, which is responsible for the observed difference in composition between the film and target.

In order to elucidate the surface related chemical characteristics of the TFMG, XPS analysis was performed on the sample. The XPS pattern (Fig. 4) of Zr 3d, 3p ,3s, Cu2p, Al 2p, Ag 3p, 3d, O 1s,C 1s etc., are detected indicating the presence of multiple elements on the surface oxide film at a depth of about 2nm. The C 1s spectrum arose from a contaminant hydrocarbon layer covering the sample surface and the O indicates that the sample surface has been partially oxidized. In the Zr spectrum (Fig.5a) Zr 3d consists of a peak at 178.89 and at 179.72 eV which can be assigned as metallic Zr^o, and the peaks at higher binding energy is 181.37 and 183.80 eV are assigned as Zr $3d_{5/2}$ and Zr $3d_{3/2}$ electrons originating from the oxidized Zr^{4+} state [36]. Zr 3p spectrum exhibits two peaks as Zr $3p_{3/2}$ and Zr $3p_{1/2}$ which has

peaks at 333.38 and 346.87 eV. As observed by Nie et al, [37] a weak Zr 3s peak was detected at 432.19 eV which is not due to metallic Zr but oxidized Zr peak form the surface. Peaks at 934.13 eV and 954.80 eV are observed on the Cu 2p spectrum region (Fig.5b) for all metallic alloys with peaks assigned as Cu $2p_{3/2}$ and Cu $2p_{1/2}$ from the spectra.

The signals centered at 944 eV and 963.9 eV are the shake-up peaks of Cu 2p arising from the interaction of the emitted photo electron with a valence electron of the Cu(II) cupric ion. The kinetic energy of the emitted photoelectron is reduced due to this interaction and is observed as a "shake-up" peak at a higher binding energy than the main line. Both cuprous Cu^{1+} and cupric Cu^{2+} ions reportedly show such satellite peaks. However, the low signal to noise ratio obtained for the Cu scan and the shape of the shake-up peaks suggests that in the sputtered film, the Cu exists in its cupric form as $Cu(OH)_2$. The satellite peak then probably arises by a charge transfer transition from the $(OH)^{2-}$ group to the unfilled d9 valence level of the cupric ion [38, 39].

Since the Al 2p spectrum is overlapped with the Cu 3p spectrum, the Al peak is originating from oxidizing state (Al^{3+}) and from Cu $3p_{3/2}$and Cu $3p_{1/2}$ electrons. The peak at 569.96 eV corresponds to the metallic 3p and the weaker Ag 3d spectrum (Fig. 5c) is deconvoluted and fitted by a single spin-orbit splitting doublet of Ag $3d_{5/2}$ at 368.7 eV and Ag $3d_{3/2}$ at 374.5 eV, which is originating from the Ag^{o} metallic state [40]. The O 1s spectrum is composed of two peaks, as shown in Fig.5d originating from oxygen in metal-O-metal bond, metal - OH bond. The lower binding energy peak at 530.0 - 531.0 eV is assigned to O^{2-} oxygen and the higher binding energy peak at 531.6 - 532.7 eV arises from OH^{-} oxygen [41]. The O^{2-} peak was more intense than the OH^{-} peak in the O 1s spectra. Therefore, the film surface consists of oxyhydroxide in which O^{2-} ions are major oxygen species. It is seen that oxidation of Zr and Al occurs in the surface of the Zr-based TFMG when they are exposed to air.

3.2. Structural properties

Figure 6 shows the XRD pattern of the Zr-Cu-Al-Ag TFMG as deposited and annealed at 450 °C (723 K) and 550 °C (823 K) on Si (100) wafer. No crystalline peak is observed in the as deposited and annealed TFMG 450 °C (723 K), but only a broad diffraction hump with a maxima at 2θ=37.50°.The XRD pattern verifies that the film is basically amorphous in nature and agrees with the diffraction hump generally observed in Zr based BMGs [42]. This indicates that the film has a glassy structure and confirms the formation of a glassy amorphous phase by the magnetron sputtering method. The film annealed at 450 °C (723 K) does not show any crystalline peak but the film annealed at 550 °C (823 K) showed a crystalline peak corresponding to the nucleation of $CuZr_2$ which is the primary crystallization phase.

Figs. 7 show the secondary electron SEM image of the surface of the Zr- based TFMG. It does show a dense film growth, but grain-like features are clearly visible under higher magnifications. Yet, the film is amorphous, as shown by XRD. Hence, these features exhibiting a dense morphology cannot be grain boundaries, but rather a surface topographical feature that evolved according to the deposition conditions. The coating whose image is shown in Fig. 7a, b was prepared at a rather high argon pressure of $3x10^{-3}$ mbar. The same film was then observed with an AFM. The surface topography of the TFMG measured by AFM in 2D, 3D modes are shown in Fig. 8a, 8b. The amorphous but fine grained structure can be noticed on the film. The width of the profile grain feature from the line profile of the film can be calculated as [43]:

$$d=4x\sqrt{(r \times R)} \quad (1)$$

where d is the apparent width of a feature, r is the sphere radius and R is the scanning tip radius which is 10nm. Here the calculated average width of the grain feature was 109.52 nm. In effect, the surface of the film comprises clusters of around 100 nm within which smaller features measuring about 10-20 nm can be discerned. Nevertheless, the deposited film has a smooth surface with an average roughness of 1.25nm (rms roughness of 1.52nm), which actually corresponds to the mean height of the feature inside the cluster.

In a recent report, Liu et al [44] carried out a similar deposition of Zr-Cu-Ni-Al TFMGs by magnetron sputtering and studied the surface topography evolution as a function of Ar pressure and sputtering power. They too reported the observation of a similar grain-like feature in their samples, even when the film remained amorphous. Since the films were not annealed, thermal stress cannot be the cause. Instead, the intrinsic stress in the film which is coupled to the working gas pressure and sputtering power can lead to such surface topographies. Low Ar pressure and high power seem to enhance surface smoothening.

Fig.9 shows a bright field TEM image of a thinned region of the specimen along with its corresponding diffraction pattern (DP). Obviously, the film did not show any crystallization behaviour in these regions confirming its glassy nature. Various regions of the film were investigated and most did not show any diffraction contrast. However, some regions under high magnification showed the presence of nano crystallites evident by the presence of diffraction rings in the DP. As Fig. 10 shows, near a hole the DP showed a spotty ring pattern (with a high background intensity arising from the amorphous matrix). The diffraction rings with d spacings of 0.271 nm, 0.196 nm, 0.169 nm and 0.142 nm were calculated and these agree with the $CuZr_2$ phase, which is the first intermetallic compound in the Zr-rich side of the Cu-Zr system. It is likely that the high overall concentration of Zr (~50 at.%) would have promoted the nucleation of the Zr rich compound first. The dark field (DF) image from one of the outer rings showed that the $CuZr_2$ nano crystallites were dispersed

randomly in the amorphous matrix in correspondence with the XRD result of the 550° C (823 K) annealed sample (shown earlier in Fig. 6). A similar crystallization sequence has been reported by Murthy and Hono [19] and also by Zhang et al [45]. While the paper by Zhang et al [45] reports on the exact eutectic composition and provides clear evidence for the formation of only $CuZr_2$ phase, [19] reports crystallization sequence in $Zr_{65-x}Cu_{27.5}Al_{7.5}O_x$ BMG that has been intentionally incorporated with oxygen. When the oxygen fraction was low ($x<0.1$), a $Zr_2(Cu,Al)$ phase was found to nucleate. However when the oxygen content was increased to 0.8, a quasi crystalline phase was found to precipitate at 673 K, which transformed to the stable $Zr_2(Cu,Al)$ after 10 minutes of ageing at 673 K. In our study, we could not detect any quasicrystalline phase nucleation, agreeing with the study by Zhang and co-workers [45]. Oh et al [15] studied phase separation in $Zr_{43}Cu_{43}Al_7Ag_7$ BMG using 3D atom probe measurements. The degree of Ag enrichment was found to be 12%. Interestingly, while their Atom Probe maps showed concentrated clusters of Ag and Cu, HRTEM showed no diffraction contrast. Based on their observations, it was suspected that the nano crystals to form first would be these pure Cu and Ag phases which when dispersed uniformly in the glassy matrix can enhance work hardening and plasticity dramatically. This tendency for phase segregation is also predicted to be the probable cause for the lowering of the crystallization energy (353 kJ/mol for $Cu_{43}Zr_{43}Al_7Ag_7$; 391 kJ/mol for $Cu_{50}Zr_{43}Al_7$). Interestingly, we did not observe any phase separation in the films into Ag or Cu clusters, by TEM. It seems that the tendency for compound nucleation precedes that for phase separation or quasicrystal nucleation. Probably, the low atomic concentration of Ag precluded its segregation, yielding to $CuZr_2$ nucleation.

Fig. 11 is a bright field image in STEM mode along with 256x256 pixel spectrum image (SI) maps obtained by analysing the XEDS lines (Zr Lα line (2.042 keV), Cu Kα (8.042 keV), Al Kα (1.486 keV), Ag Lα (2.984 keV), Si Kα (1.739 keV) and the O Kα line at

0.425 keV). As is evident from the images, the films were quite homogenous and no segregation was discernible in the maps. The interface was slightly enhanced in oxygen, arising from the native SiO_2 layer. The STEM was then switched to the spot mode and X-ray spectra were collected at discrete points and analysed across a line spanning the substrate to the film. Each spot was analysed for 30 seconds in which time the highest intensity peak exceeded 10^4 cps. The Cliff-Lorimer method was then used for quantification from the X-ray intensity profiles.

As shown in Fig. 12, the line scan across the interface of the sample showed very low inter-diffusion between the film and the substrate. Oxygen segregation is suggestive of SiO_2 formation at the surface of the nascent Si substrate. Across the oxygen-rich layer, a gradient of Si and film could be observed. As an approximation, the data were fitted to an expression of the type $C_0\exp(-x^2/2Dt)$, which is a solution to the diffusion equation in the thin film approximation. While this approach is not strictly exact, calculation of the FWHM (w) of Si and Zr yielded values of 39.5 nm and 25 nm respectively. Both these values lie within the oxygen enhanced SiO_2 region observed in the SI maps indicating low inter-diffusion between the film and the substrate.

3.4. Mechanical properties

Thickness of the coating as determined from Calo test was found to be 0.56 micron as shown in Fig. 13. Scratch resistance of the samples was tested and the results along with the microscopic image of the tested surface are shown in Fig. 14 respectively. The test involves generating a controlled scratch with a diamond tip on the sample under either constant or progressive load. Acoustic, friction and tip position data are collected by appropriate sensors attached to the indenter holder. The failures of the coating, corresponding to different mechanisms, reflect in the data recorded by the sensors. The critical loads (Lc) at the

initiation of these failures are used to quantify the adhesive properties of the film on the given substrate. The initiation of crack and de-lamination are marked by a sudden change in friction. The preceding crest of the event in the friction graph is taken as the corresponding Critical Load. As the friction values may fluctuate due to the presence of particle debris and local irregularities, the critical loads are reconfirmed using the acoustic data. The acoustic emission will show a dip associated with the event. The failure events are verified using the penetration depth profile as well as with the help of optical microscopy, by examining the image of the scratch.

The critical loads are an indicator of the scratch resistance of the samples. If the critical load is higher, more force has to be applied to the sample for the failure, meaning that the sample is more resistant. The critical loads for the first crack event (Lc1), first de-lamination (Lc2) and total de-lamination (Lc3) were determined by means of the frictional force and acoustic emission data. The critical loads corresponding to Lc1 ; Lc2 ; Lc3 are 1.33±0.19 N, 1.69±0.13 N, 9.30±0.93 N respectively for the TFMG coated onto stainless steel substrate are measured. The observed higher critical load of Lc3 clearly shows that the specimen is more resistant to scratches and cosmetic defects.

4. Conclusions

Multi component thin film metallic glasses of $Zr_{48}Cu_{36}Al_8Ag_8$ were synthesized using single –target magnetron sputtering onto Si (100) wafers and SS substrates. The amorphous $Zr_{48}Cu_{36}Al_8Ag_8$ TFMG exhibits a wide super cooled liquid region (ΔT_x) of about 83 K indicating the high thermal stability and high stabilization against crystallization. The amorphous TFMG consist of a single glassy phase, as evidenced by a broad diffraction hump and no detectable peaks corresponding to crystalline phases as observed from XRD. Elemental composition close to the target alloy was noticed from EDS analysis and the XPS

analysis indicates the presence of Zr, Cu, Al, Ag, O, C on the surface oxide film at a depth of about 2nm. Under high magnification in some regions TEM shows the presence of nano crystallites belonging to $CuZr_2$ phase. A smooth morphology with an average roughness of 1.25 nm and grain-like features were observed from AFM and SEM analysis. The specimen is highly resistant to scratches and cosmetic defects as observed from the scratch test.

Acknowledgement

Author acknowledges CSIR-CECRI, Karaikudi and CSIR, New Delhi for the award of research grant under M2D programme - CSC0134 to carry out this work. Author thanks Prof. Akira Kobayashi and Prof. M. Takahashi of Osaka University, Japan for the STEM and experiments. Acknowledgements are due to Er C.V. Muraleedharan of Sree Chitra Tirunal Institute for Medical Sciences and Technology, Thiruvananthapuram for the mechanical properties measurement. Authors thank the Director, CSIR-CECRI and Dr M.Jayachandran, Head of Electrochemical Materials Science Division of Central Electrochemical Research Institute, Karaikudi for their continuous encouragement.

References

[1] Mingwei Chen, *NPG Asia Mater*. 2011, **3**, 82-90.

[2] H. W. Sheng, W. K. Luo, F. M. Alamgir, J.M. Bai, E. Ma, *nature* 2006, **439**, 419 -425.

[3] A. Inoue, A. Takeuchi, *Acta Materialia,* 2011, **59,** 2243-2267.

[4] X.H. Lin, W.L. Johnson, *J. Appl. Phys*., 1995, **78**, 6514-6519.

[5] Alain Reza Yavari*, nature,* 2006, **439**, 405-406

[6] Marie E. Coxa, Laszlo J. Kecskesb, Suveen N. Mathaudhuc, David C. Dunanda, Materials Science and Engineering A, 2012, **533,** 124-127.

[7] Jason S. C. Jang, M. T. Chen, Y. W. Chen, M. C. Yea, S. T. Chung, and Weite Wu, *Materials Science Forum,*2003, **426-432**, 1879-1884;

[8] Jason S. C. Jang, Y. W. Chen, L. J. Chang, H. Z. Cheng, J. C. Huang, and C. A. Tsao, *J. of Materials Chemistry and Physics*, 2005, **89**, 122-129.

[9] Qingsheng Zhang, Wei Zhang and Akihisa Inoue, *Scripta Materialia,* 2006, **55**, 711-713.

[10] Q.K. Jiang, X.D. Wang, X.P. Nie, G.Q. Zhang, H.Ma, H.-J. Fecht, J. Bendnarcik, H. Franz, Y.G. Liu, Q.P. Cao, J.Z. Jiang, *Acta Materialia*, 2008, **56,** 1785-1796.

[11] B. Li, J.S.C. Jang, S.R. Jian, K.W. Chen, J.F. Lin and J.C. Huang, *Materials Science and Engineering A,* 2011, **528,** 8244-8248.

[12] Huei-Sen Wang, Mau-Sheng Chiou, Hou-Guang Chen, Jason Shian-Ching Jang, Jhen-Wang Gu, *Intermetallics*, 2012, **29,** 92-98.

[13] Mitsuhiro Watanabe, Shinji Kumai, Go Hagimoto, Qingsheng Zhang, Koji Nakayama, *Materials Transactions*, 2009, **50**, 1279-1285.

[14] Q.K. Jiang, X.D. Wang, X.P. Nie, G.Q. Zhang, H. Ma, H.-J. Fechtd, J. Bendnarcik, H. Franz, Y.G. Liu, Q.P. Cao, J.Z. Jiang, *Acta Materialia,*2008, **58**, 1785-1796

[15] J.C. Oh, T. Ohkubo, Y.C. Kim, E. Fleury, K. Hono, *Scripta Materialia,*2005, **533**, 165-169

[16] G. A. Almyras, G. M. Matenoglou, P. Komninou, C. Kosmidis, P. Patsalas, G. A. Evangelakis, *J.Appl. Phys*., 2010, **107**, 084313(1-6).

[17] R. Yamauchi, S. Hata, J. Sakurai, A. Shimokohbe, *Jap. J. Appl. Phys*. 2006, **45**, 5911-5919.

[18] Ching-Yen Chuang , Jyh-Wei Lee , Chia-Lin Li , Jinn P. Chu, *Surface & Coatings Technology*, 2013,**215**, 312-321.

[19] Jinn P. Chu, J. S. C. Jang, J. C. Huang, H. S. Chou, Y. Yang, J. C. Ye, Y. C. Wang, J. W. Lee, F. X. Liu, P. K. Liaw, Y.C. Chen, C.M. Lee, C.L. Li, C. Rullyani, *Thin Solid Films,*2012, **520**, 5097-5122.

[20] Y.H. Liu, T. Fujita, A. Hirata, S. Li, H.W. Liu, W. Zhang, A. Inoue, M.W. Chen, *Intermetallics,*2012, **21**, 105-114.

[21] C.H. Huang, J.C. Huang, J.B. Li, J.S.C. Jang, *Materials Science and Engineering C*, 2013, **33**, 4183-4187.

[22] B. S. Murty and K. Hono, *Mater. Sci. Eng. A*, 2001, **312**, 253-261.

[23] J.B. Li, J.S.C. Jang, S.R. Jian, K.W. Chen, J.F. Lin, J.C. Huang, *Materials Science and Engineering A*, 2011, **528,** 8244-8248

[24] Qing-sheng Zhang, Wei Zhang, Guo-qiangXie, and Akihisa Inoue,*International Journal of minerals, Metallurgy and Materials*. 2010, **17**, 208- 213.

[25] Huei-Sen Wang, Mau-Sheng Chiou, Hou-Guang Chen, Jason Shian-Ching Jang, Jhen-Wang Gu, *Intermetallics*, 2012, **29,** 92-98.

[26] Qingsheng Zhang, Wei Zhang and Akihisa Inoue,*Scripta Materialia,* 2006, **55**, 711-713.

[27] J. Sort, N. Van Steenberge, A. Gimazov, A. Concustell, S. Suriñach, A. Gebert, J. Eckert and M.D. Baró. *The Open Materials Science Journal*, 2008, **2**, 1-5

[28] Wei he, Andrew Chuang, Zheng Cao, and Peter K. Liaw.*Metallurgical and materials transactions A*, 2010, **41**,1726-1734.

[29] Chen Qi, Liu Lin, K.C. Chan ,*Sci china Ser g-Phys MechAstron*., 2008 , **51** , 349-355

[30] ZongHaiTao, ZhangXinYu, LiLiXin, BianLinYan, Liang Shun Xing, Tan Chun Lin, *ChinSci Bull*., 2012, **57**, 1219-1222.

[31] Y. T. Shen, L. Q. Xing and K. F. Kelton, *Philosophical Magazine*, 2005, **85**, 3673-3682.

[32] Hisamichi Kimura, MichioKishida, Takejiro Kaneko, Akihisa inoue and Tsuyoshi Masumoto, *Materials Transaction*, *JIM*, 1995, **36**, 890-895.

[33] Li Gong, LiuRiPing, LiYanChun, Liu Jing, *Chinese Sci Bull.,*2011, **56**, 4-5.

[34] A. Concustell, M. Zielinska, A´.Re´ve´sz, L.K. Varga, S. Surinach, M.D. Baro, *Intermetallics,* 2004, **12**, 1063–1067.

[35] W.H. Wang, J.J. Lewandowski, A.L. Greer, *J. Mater. Res*., 2005, **20**, 2307-2313.

[36] Asahi Kawashima, Kazuyo Ohmura, Yoshihiko Yokoyama, Akihisa Inoue. *Corrosion Science,* 2011, **53**, 2778-2784.

[37] X.P. Nie, X.H. Yang, Y. Ma, L.Y. Chen, K.B. Yeap, K.Y. Zeng, D. Li, J.S. Pan, X.D. Wang, Q.P. Cao, S.Q. Ding, J.Z. Jiang *, Intermetallics*, 2012, **22,** 84-91.

[38] J. Hernandez, P. Wrschka, and G. S. Oehrlein, *Journal of The Electrochemical Society*, 2001, **148,** G389-G397.

[39] M.C. Biesinger, L.W.M. Lau, A.R. Gerson, R.St.C. Smart, *Appl. Surf. Sci*. 2010, **257,** 887-898.

[40] Nengbin Hua, Lu Huang, Jianfeng Wang, Yu Cao, Wei He , Shujie Pang, Tao Zhang . *Journal of Non-Crystalline Solids,* 2012, **358,** 1599-1604.

[41] K. Asami, K. Hashimoto, S. Shimodaira, *Corros. Sci.,* 1977, **17,** 713-723.

[42] Y.H. Liu, T.Fujita, A. Hirata, S. Li,H.W. Liu, W. Zhang,A. Inoue, M.W. Chen, *Intermetallics,* 2012, **21,** 105-114.

[43] B. Subramanian, R. Ananthakumar, S. Yugeswaran, M. Jayachandran, M. Takahashi, Akira Kobayashi, *Vacuum*, 2013, **88,** 108-113.

[44] Y.H. Liu, T. Fujita, A. Hirata, S. Li,H.W. Liu, W. Zhang, A. Inoue, M.W. Chen. *Intermetallics*, 2012, **21,** 105–114.

[45] Q.S. Zhang, W. Zhang, G.Q. Xie and A. Inoue, *Journal of Physics: Conference Series* 2009, **144,** 012031.

Figure captions

Figure1. (a) DSC thermogram of $Zr_{48}Cu_{36}Al_8Ag_8$ TFMG, (b) DSC thermogram showing melting temperature and liquidus temperature of $Zr_{48}Cu_{36}Al_8Ag_8$ TFMG.

Figure 2a. Crystallization temperature, T_x of various compositions of Zr based metallic glasses.

Figure 2b. Glass transition temperature, T_g of various compositions of Zr based metallic glasses.

Figure 3. EDAX spectrum of $Zr_{48}Cu_{36}Al_8Ag_8$ TFMG

Figure 4. XPS of the $Zr_{48}Cu_{36}Al_8Ag_8$ TFMG surface.

Figure 5. XPS deconvoluted spectra for (a) Zr 3d (b) Cu 2p (c) Ag 3d (d) O1s

Figure 6. X-ray diffraction pattern of $Zr_{48}Cu_{36}Al_8Ag_8$ TFMG.

Figure 7. SEM images of the surface of the $Zr_{48}Cu_{36}Al_8Ag_8$ TFMG indifferent magnification.

Figure 8a. Surface topography of $Zr_{48}Cu_{36}Al_8Ag_8$ TFMG in 2D view.

Figure 8b. Surface topography of $Zr_{48}Cu_{36}Al_8Ag_8$ TFMG in 3D view.

Figure 9. Bright field TEM image of a thinned region of the specimen along with its corresponding diffraction pattern.

Figure 10. (a) Bright field image of a plan view sample near a hole, (b) corresponding diffraction pattern showing calculated *d* spacings in nm and (c) a dark field image taken from the continuous ring in (b).

Figure 11. A bright field S-TEM and X-ray spectral image maps across a TFMG/substrate region.

Figure 12. Interface composition obtained by XEDS point analysis in the S-TEM.

Figure 13. Optical image of the calo tested sample showing two concentric rings and exposed substrate.

Figure 14. Results of the scratch test showing variation of the normal force, frictional force, friction coefficient and acoustic emission with load.

Table 1. Deposition parameters employed for the sputtering process

Deposition parameters	
Target	$Zr_{48}Cu_{36}Al_8Ag_8$
Substrate	Silicon, quartz
Target-Substrate distance	6 cm
Substrate temperature	Room temperature
Base pressure	$8x10^{-6}$ mbar
Working pressure(Ar)	$3x10^{-3}$mbar
Power	30 watt
Deposition time	2 hours

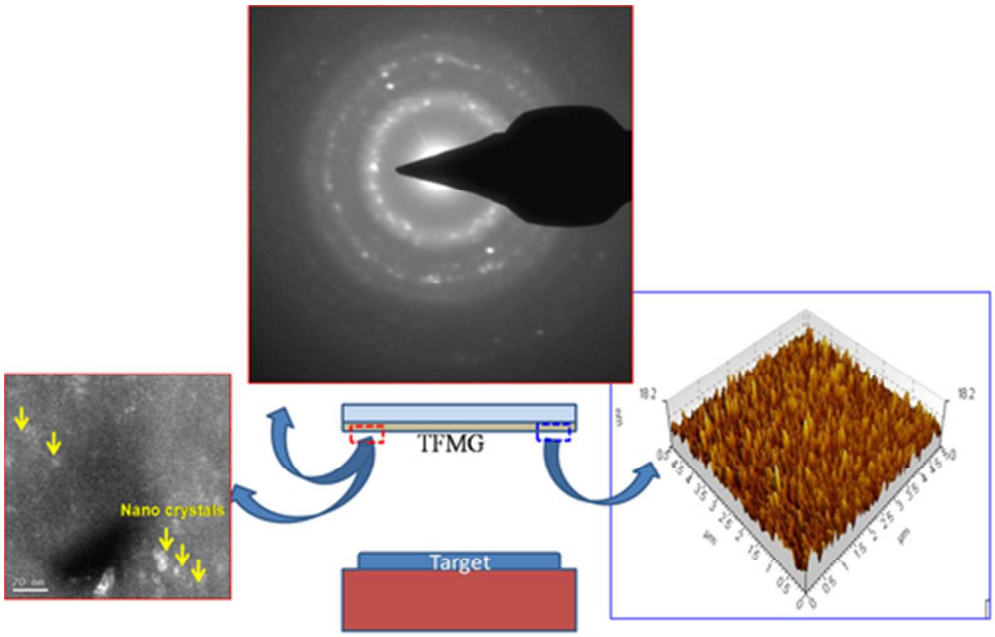

Graphical Abstract
42x27mm (300 x 300 DPI)

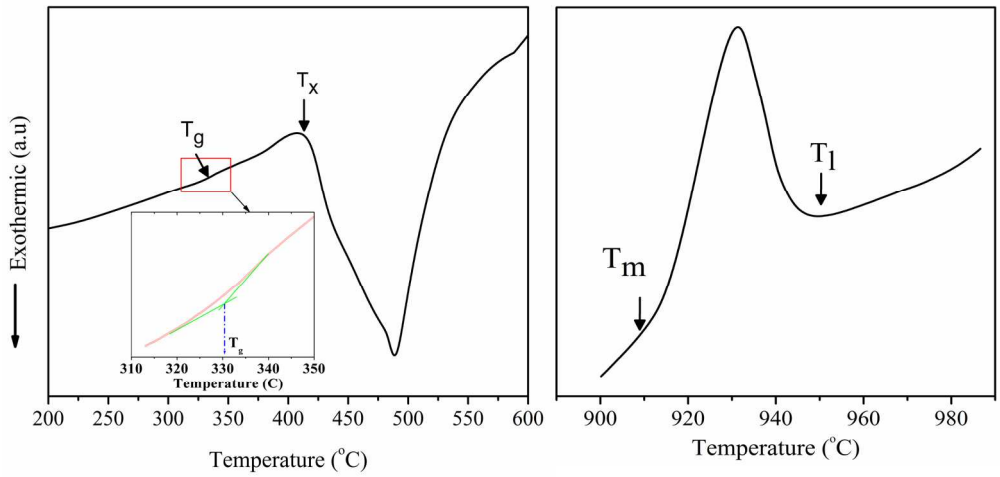

Fig. 1
175x83mm (300 x 300 DPI)

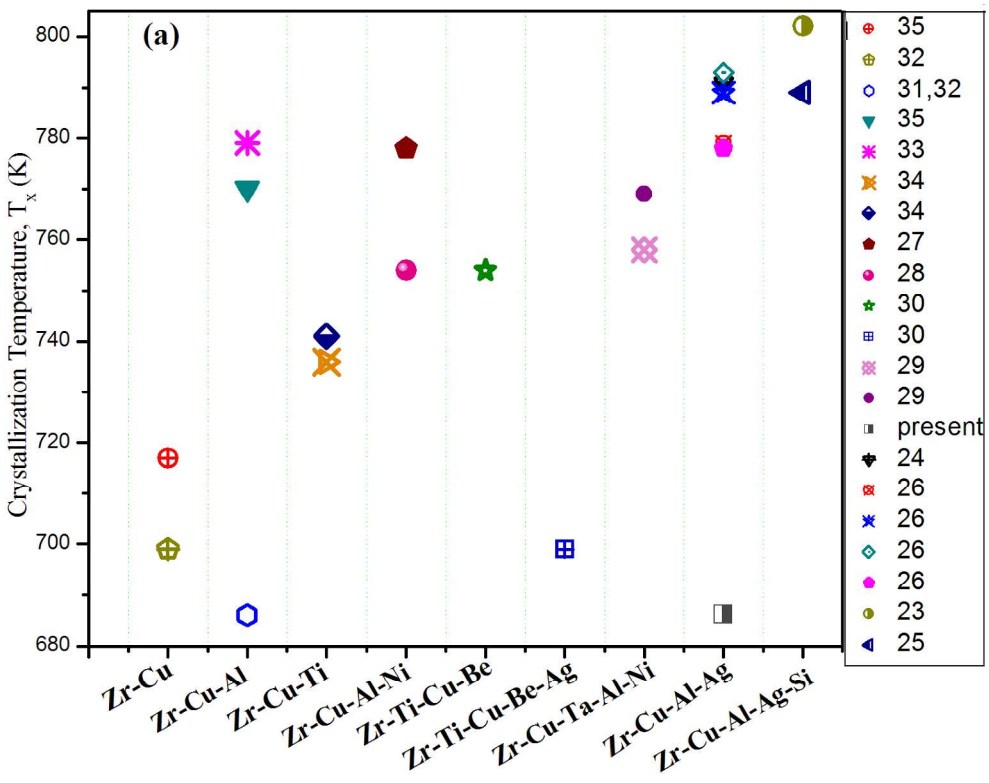

Fig.2a
279x215mm (300 x 300 DPI)

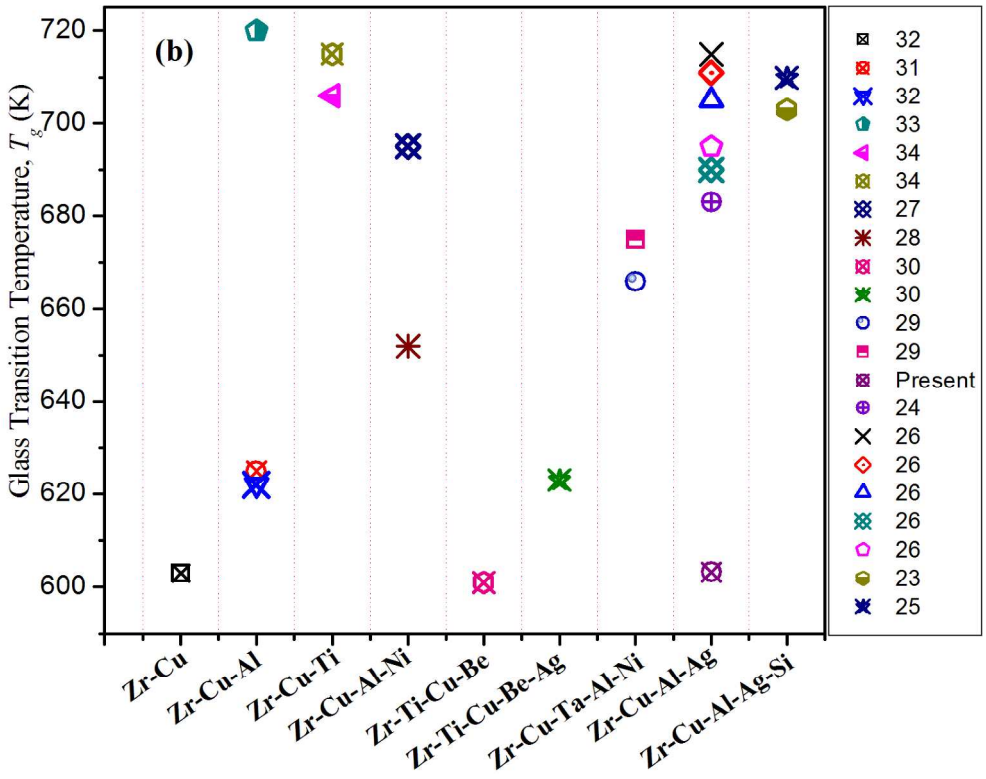

Fig.2b
279x215mm (300 x 300 DPI)

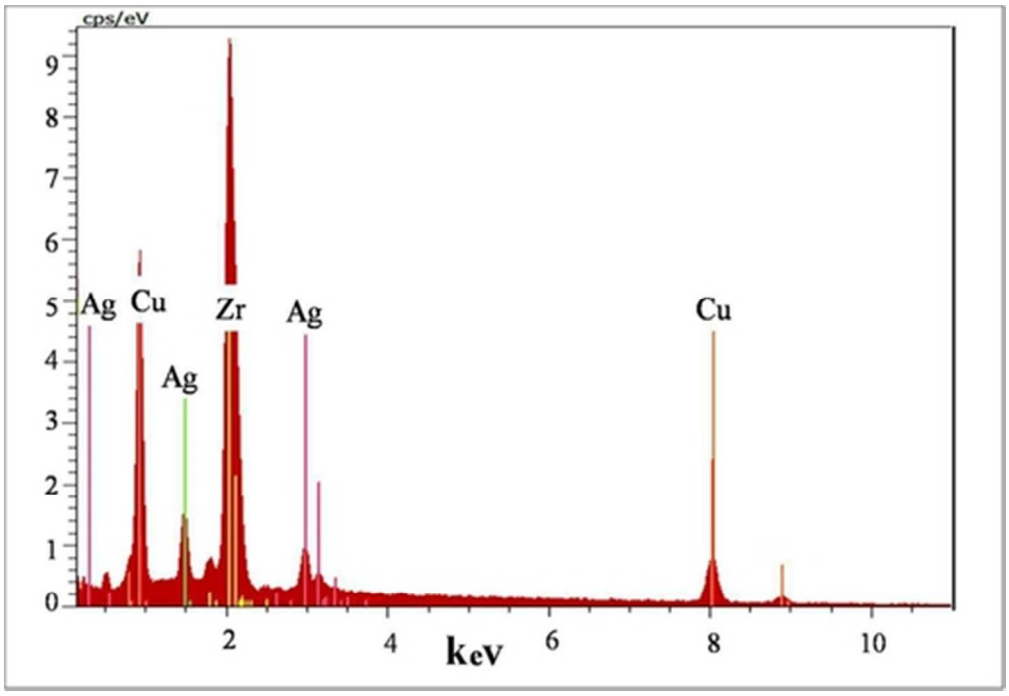

Fig. 3
43x29mm (300 x 300 DPI)

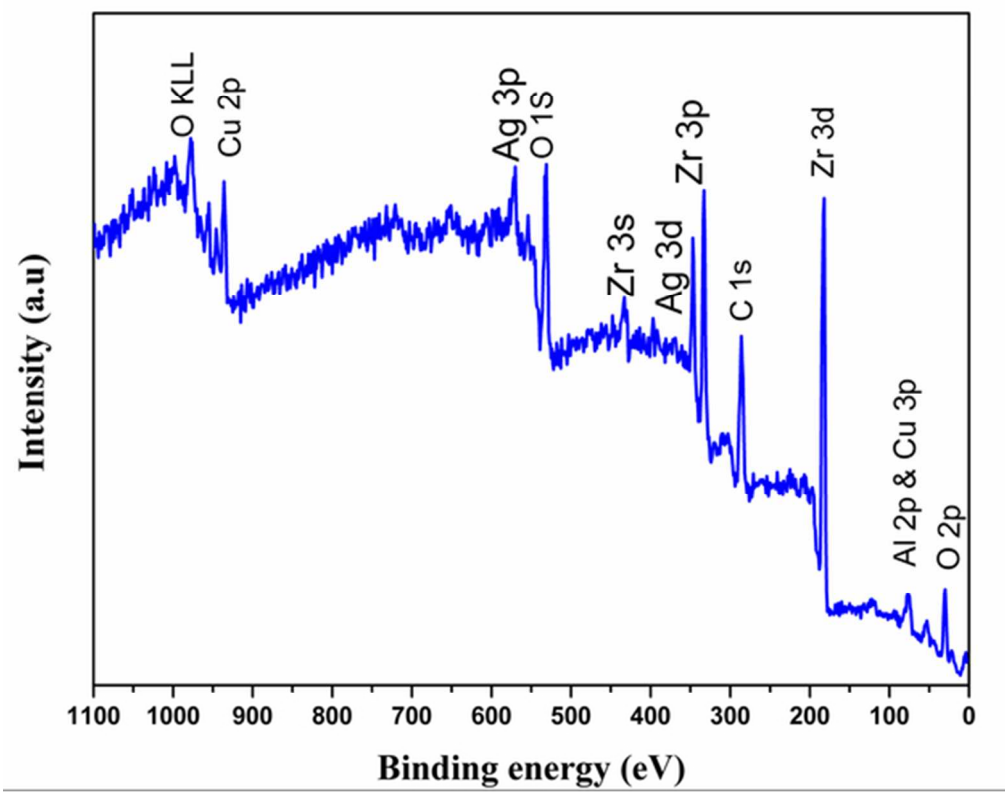

Fig. 4
52x41mm (300 x 300 DPI)

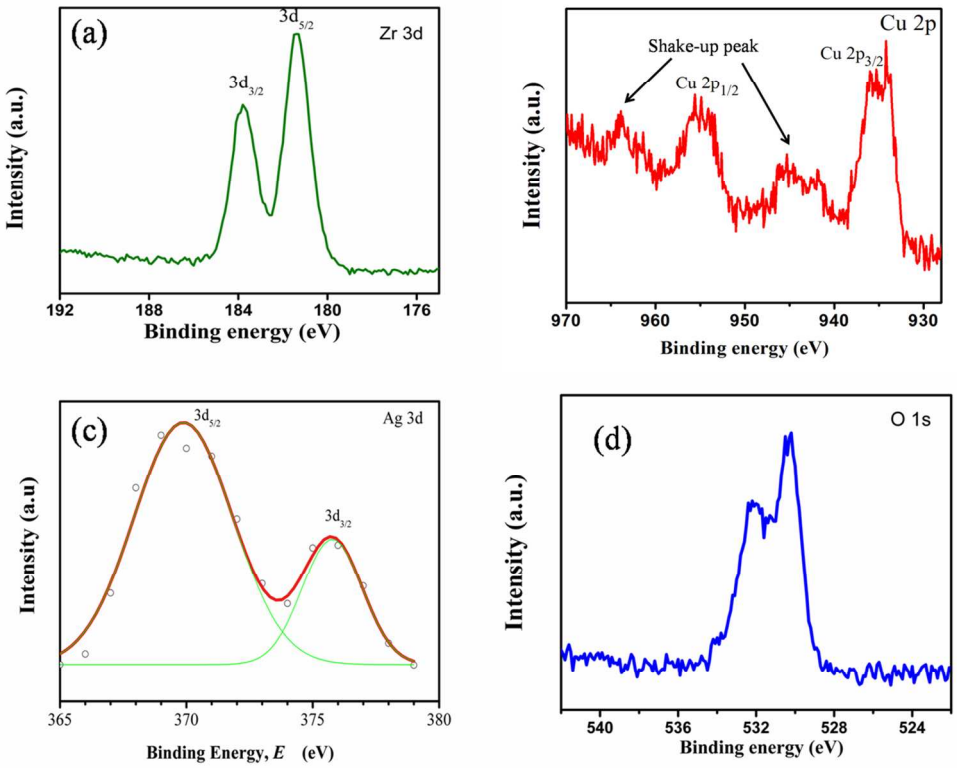

Fig. 5
118x93mm (300 x 300 DPI)

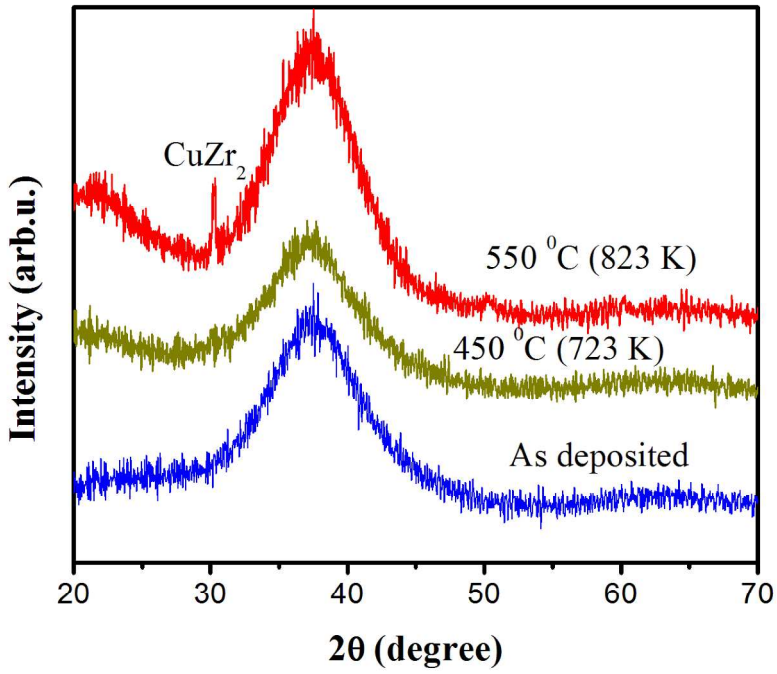

Fig.6
279x215mm (300 x 300 DPI)

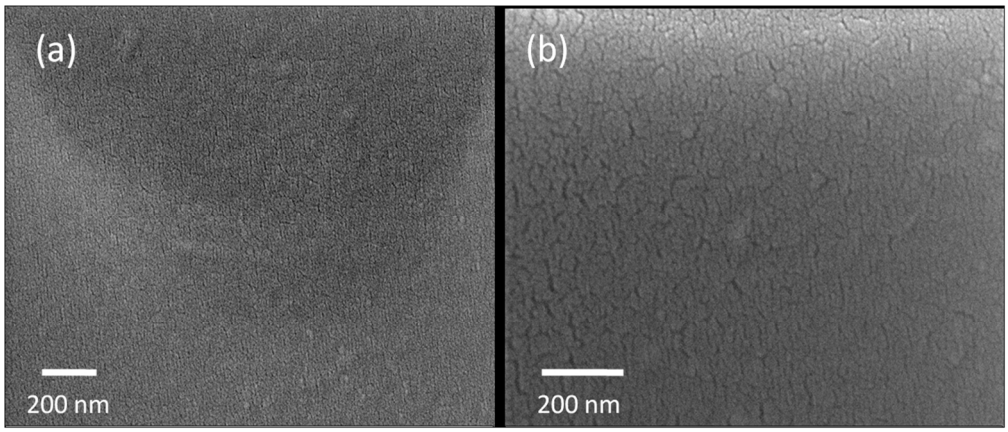

Fig. 7
116x49mm (300 x 300 DPI)

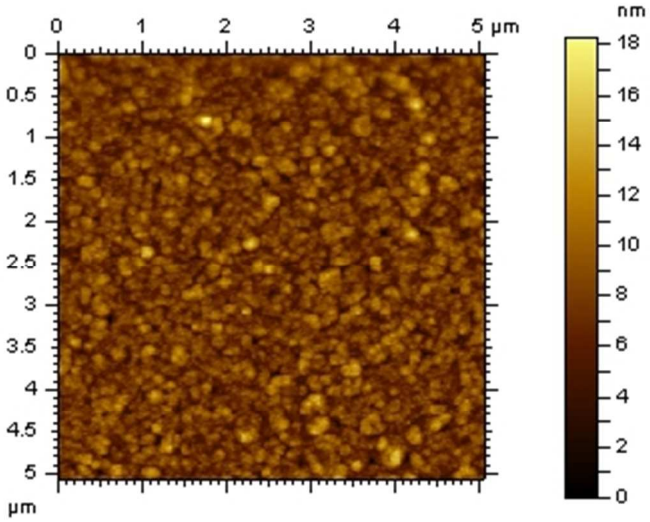

Fig. 8a
96x76mm (96 x 96 DPI)

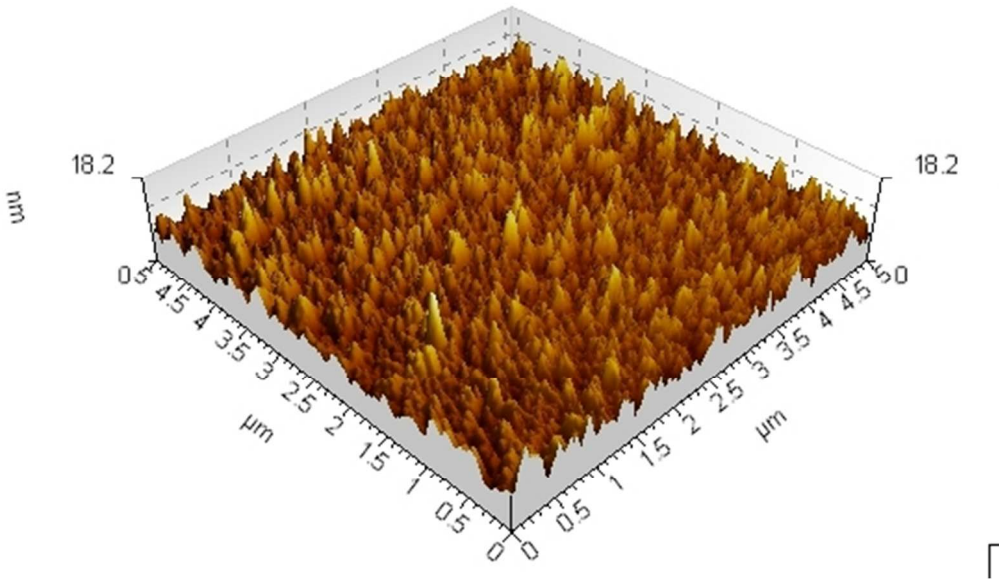

Fig. 8b
142x85mm (96 x 96 DPI)

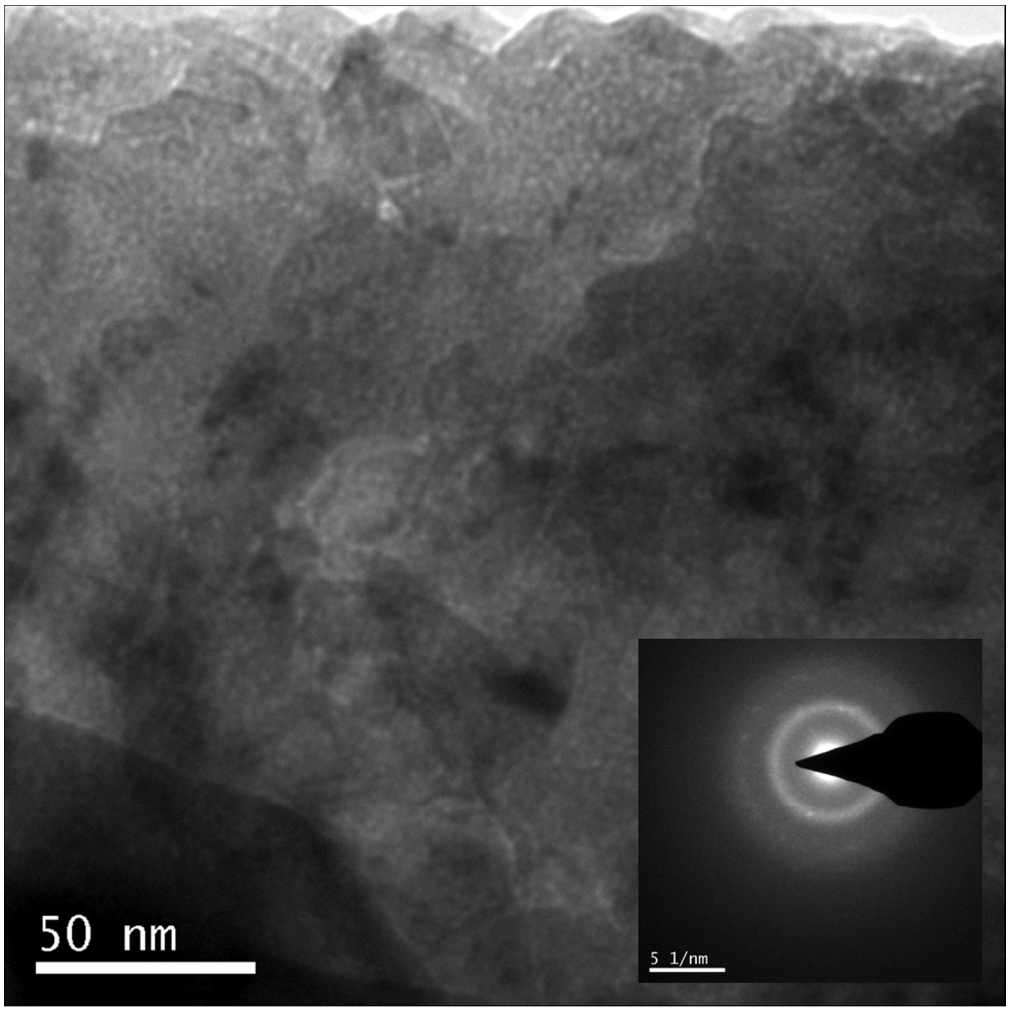

Fig. 9
190x190mm (150 x 150 DPI)

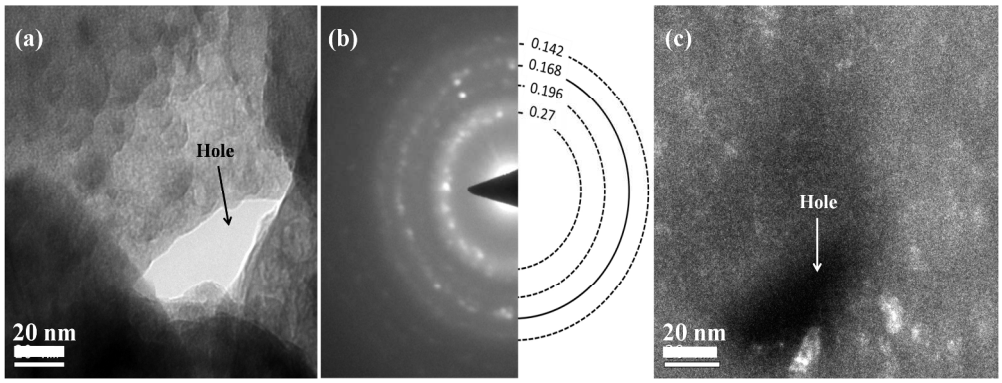

Fig. 10
256x95mm (300 x 300 DPI)

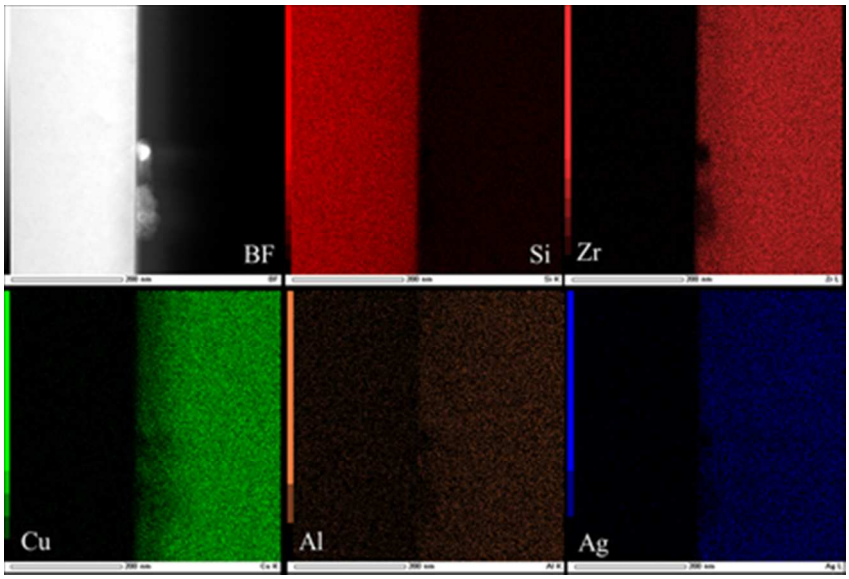

Fig. 11
35x24mm (300 x 300 DPI)

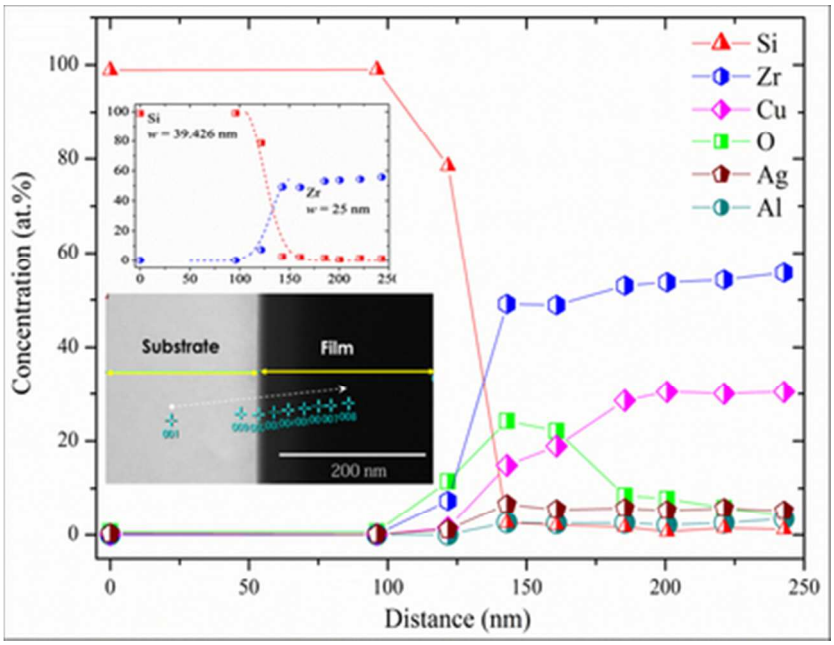

Fig. 12
34x26mm (300 x 300 DPI)

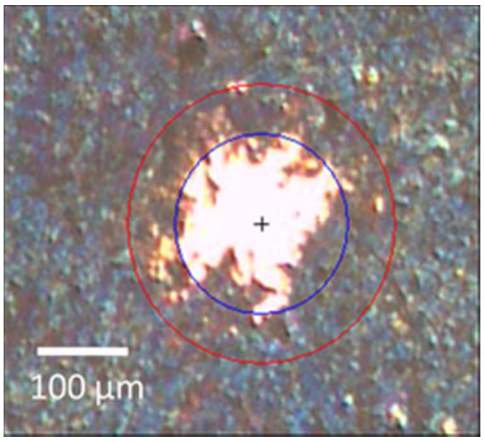

Fig. 13
20x18mm (300 x 300 DPI)

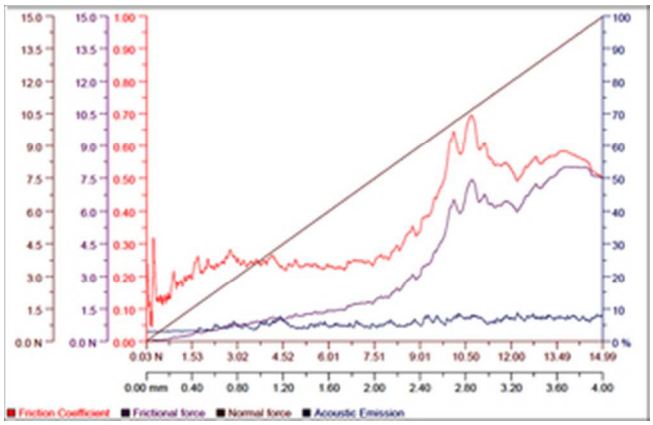

Fig. 14
27x17mm (300 x 300 DPI)